TERMINAL BALLISTICS APPLICATION OF X-RAY COMPUTED TOMOGRAPHY (XCT) FOR THE QUANTITATIVE IN-SITU ANALYSIS OF FRAGMENTS EMBEDDED IN COLLECTION MEDIA

Uta Gabriel[1], Gilles Pageau[2], Mathieu Des Roches[3], Simon Ouellet[4]
Yves Baillargeon[4], Pierre Francus[3] and Nicholas Shewchenko[5]
[1]*Numerica Technologies Inc., Quebec City, Quebec, Canada*
[2]*Calian Group Ltd, Quebec City, Quebec, Canada*
[3]*Institut National de la Recherche Scientifique, Quebec City, Quebec, Canada*
[4]*Defence R&D Canada, Quebec City, Quebec, Canada*
[5]*Biokinetics and Associates Ltd., Ottawa, Ontario, Canada*

The characterization of fragmenting munitions involves conducting arena tests with witness materials (e.g. plywood) to collect fragments. The evaluation of body armour against buried explosives follows a similar process where surrogates made of foam or gel are used to support the armour and capture penetrating soil debris. The manual recovery of the collected fragments is long, tedious and prone to error since small fragments are often not detected. The effectiveness of XCT as a rapid non-destructive technique was evaluated by scanning calibration targets containing various objects of known material types, sizes, and locations. The *Fragfinder* program was developed to automatically perform 3D images analysis. All fragments were detected and accurately located. For lower density materials (glass, aluminum, titanium), the relative error on the volume of the fragment was within 8%. For higher density materials, (steel, tungsten), larger errors were obtained because of image reconstruction artifacts. Finer reconstruction of target scans using smaller voxel sizes along with artifacts reduction algorithms were explored in order to obtain better precision.

INTRODUCTION

Fragmenting warheads are usually characterized by performing static arena tests [1] where witness panels, typically made of fiberboard or plywood panels, are deployed on a fixed radius around the bursting munition. Panels are recovered post-detonation for subsequent analysis, where individual fragments are collected manually counted and described by their coordinates, material type, entry hole dimensions, shape, mass, and depth of penetration (DoP). The direction and impact velocity of each individual fragment is determined from the impact conditions and DoP calibration equation [2-4]. The data can then be use as input for vulnerability models [5] in order to evaluate the lethality of the warhead and/or help with the design of protection systems. The evaluation of the effectiveness of Personal Protective Equipment (PPE) against buried explosive charges follows a similar process where the ejected soil debris is the fragmentation threat to characterize and mitigate (Figure 1) [6-10]. Human body surrogates (simplified or with an anthropomorphic shapes) made of various materials (e.g. foams, woods, and gels) [11] can be used to support the armour and capture incoming soil particles, pebbles and rocks.

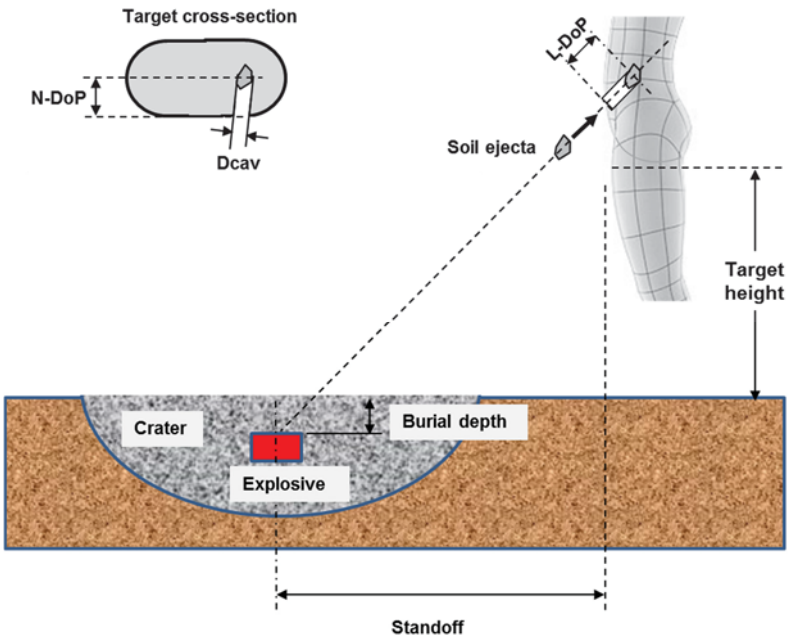

Figure 1. Typical set-up for buried explosive testing of PPE.

A key difference between munitions and buried explosive arena tests is the nature of the fragment collection media. Fragmenting munitions require a relatively strong media [12] capable of stopping high-velocity metallic fragments whereas soil ejecta require a softer medium capable of capturing brittle fragments without breaking or eroding them. Also, since the compliance of the material supporting any PPE is known to influence its ballistic performance [13, 14], it is preferable to use a material that is representative of the underlying body [15]. When testing PPE over witness packs, bare (without PPE) packs are typically collocated to allow for differential injury/casualty reduction assessment.

Manual post-test analysis of witness/surrogate systems is very time consuming, therefore expensive, and destructive. It is also prone to error since small fragments are often not detected, or recovered. Human body surrogates with a simplified geometry (i.e. not anthropomorphic) can be made of layered materials to facilitate dissection and the recuperation of fragments. However, this remains a long process and it limits the accuracy of measurement of DoP.

This study aims at evaluating the feasibility and accuracy of medical XCT scanner in numerically locating and describing fragments within exposed witness packs. First, in order to help assessing the required XCT resolution for the measurement of fragment volume (*Vol*) and DoP, a sensitivity analysis was performed with a real witness pack made of ten 9.5 mm layers of SC42 foam which had been impacted by real rock fragments. This particular pack configuration was previously calibrated by firing, in the lab, individual rock fragments of 4 mass groups (0.13, 0.3, 1 and 5 g) with sizes ranging from 2.5 to 16 mm. A general linear regression of all the data was performed (Figure 2, left) on the relationship between impact velocity (*V*) and the normalized DoP. The normalized DoP was obtained by dividing DoP by the diameter (*D*) of an equivalent sphere of same mass and density ($\rho = 2.7$ g/cm^3) as the individual rock fragment. This is in-line with the penetration models proposed by Wijk [16], Heine [17], and Cunniff [18], where projectile sectional density (*S*) is used for normalization, which for a sphere is essentially the same since: $S = M/A = (2/3)*\rho*D$.

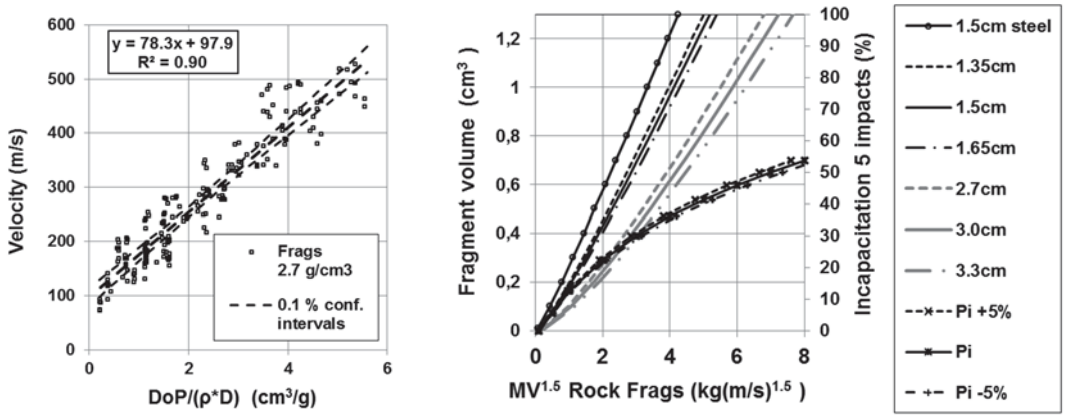

Figure 2. Normalized DoP-velocity function (left); Incapacitation vs ballistic dose ($MV^{1.5}$, right).

The resulting linear equation can then be applied to any density of projectile with the pack penetration threshold velocity (*V* at DoP = 0) being inversely proportional to *S,* as per the model by Sperrazza [19]. For the sensitivity study, an injury metric called the ballistic dose ($BD=M*V^{1.5}$) [20] was calculated for two nominal DoP (1.5 & 3cm ±10%) and a range of fragment volumes. As seen in Figure 2 (right), the ballistic dose is more sensitive to variations in DoP than in *Vol,* which is expected since: $BD \approx Vol^{0.5}*Dop^{1.5}$. A higher resolution on DoP measurements is therefore more desirable. The probability of incapacitation computed using the Kokinakis model [21] (5 impacts pelvis/defence) is also shown to not be very sensitive to variations in ballistic dose.

CALIBRATION AND WITNESS TARGETS DESCRIPTION

A number of dedicated calibration or reference objects [22] have been developed by other authors to verify the accuracy and repeatability of the measurements made using a XCT system. However for this study, three custom calibration packs that were more relevant to our specific application were designed for assessing the location and volume resolution capability of our XCT system (TABLE I). An additional witness pack from a live fire tests was also included in the study. The first calibration target was made of foam layers [15]. Within the foam target, 17 aluminum parts and 3 sizes of glass spheres were embedded in a regular pattern, with one piece of each shape in each of the 16 foam layers. The second calibration target was a lower torso model (Figure 3) molded using a 20% ballistic polymer gel (Clear Ballistics™), which included the same 20 shapes as in the foam target (Figure 4) but with 4 additional objects (i.e., a large glass sphere (ID 21), a glass-bonded mica cylinder (Mycalex® MM500, ID 0) and the two parts of an aluminum bookbinding screw (complex objects ID 22 & 23)). The third calibration target was made of Plywood. It had 46 different embedded objects. These were composed of several materials (Al, Ti, Glass, steel, tungsten) and represented different shapes including standard fragment simulating projectiles (FSP). Although the plywood calibration target included 5 sections (Figure 5), only the last (mixed materials) section representing a more complex case than normally encountered was analyzed in the present study. The CT-Scan and analysis were performed twice (Figure 5). The first scan was done with the target original width (610 mm) which required the use of the

CT scanner extended field of view option. The second scan was performed with a reduced field of view width (430 mm) to quantify the loss of resolution caused by the extended field of view.

TABLE I. CALIBRATION TARGETS AND WITNESS PACK DESCRIPTION.

Name	Fragments	Form/Description
Foam calibration	320 objects, 20 shapes aluminum, Mycalex, glass	Square, 16 layers 6.35mm thick (406 x406x114mm)
Gel torso calibration	159 objects, 24 shapes aluminum, Mycalex, glass	Lower torso/upper leg model (300x440x460mm))
Plywood calibration	640 objects, 46 shapes, glass, aluminum, titanium steel, tungsten	Rectangular, 8 layers 19mm thick, 5 sections (152x2440x430/610mm reduced/full width)
Plywood witness pack	11 munition fragments	Rectangular, 8 layers 19mm thick (152x1220x610mm)

Figure 3. Torso gel target (FaroArm® used for precise location measurement: left, CT scan: right).

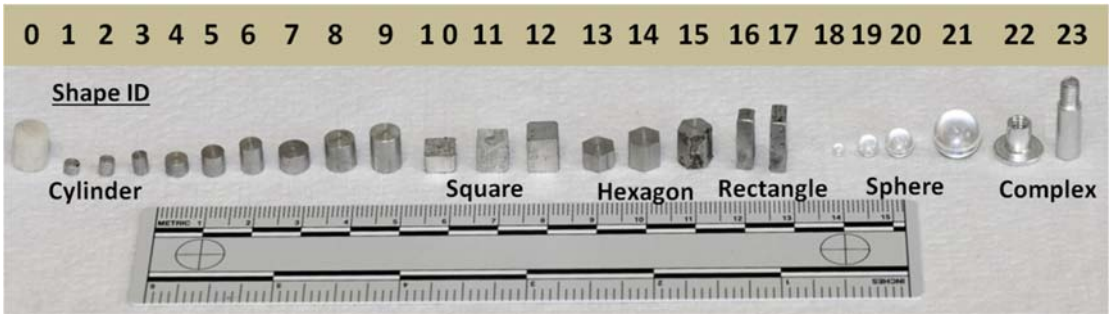

Figure 4. Fragments contained in foam and torso gel calibration targets (shape no on top).

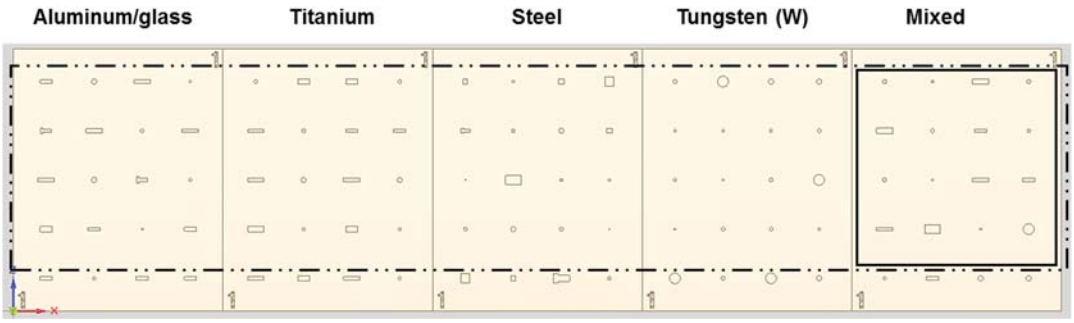

Figure 5. Fragment configuration for layer 1 of plywood calibration target with 5 zones.

X-RAY COMPUTED TOMOGRAPHY METHOD AND ANALYSIS

XCT was introduced in the early 1970s for medical imaging to supplement standard radiographs and ultrasound. XCT uses X-rays for creating thin 2D cross-sections of a physical object that are combined to recreate a virtual 3D model. Nowadays, XCT is used for industrial [23], wound [24-26] and terminal ballistics [27-28] applications. Many hardware and software advances are still on the horizon for enhancing the quality and performance of CT images and addressing the impairing artifacts (noise, motion, and metal artifacts) [29].

Image acquisition for the four targets was performed at INRS, Quebec City, using a Siemens Somatom Definition AS+128 medical CT-scanner. The main specifications of the CT-scanner and optimal parameters used are given in TABLE II. The Siemens system integrates the *syngo.*via® imaging software for X-ray scan control, with the SAFIRE and MARIS algorithms for iterative reconstruction and metal artifact reduction. Scanning was done with the coronal plane of all samples aligned with the CT radiation isocenter in about 40 seconds for the foam and gel targets, and for each zone of the plywood calibration target (Figure 3, right).

CT image reconstruction is the mathematical process for converting the scan data into digital images by stacking the individual axial slices one each other and creating a matrix of 3D rectangular boxes (voxels). For the foam and gel calibration targets, the level of attenuation of the X-ray beam at each voxel, represented as gray levels, is expressed in a scale of arbitrary units (Hounsfield units HU) where the attenuation of water is nul (HU=0), air is negative (HU=-1000) and the maximum value is HU=3071. For the plywood targets, the regular and an extended scale (HU = 10000 to 30710) was used to avoid signal saturation for steel and tungsten fragments. The voxel size in each slice/axial plane can be calculated by dividing the display field of view by the number of elements (512 or 1024) in the reconstruction matrix with the voxel depth corresponding to the slice thickness. Spatial resolution achievable does not solely depend on voxel size but also on voxel blurring due to focal spot enlargement.

Although a number of commercial (*VGStudio MAX*) and freeware (*ImajeJ*) software packages are available for volumetric visualization and segmentation of the reconstructed XCT data, a custom stand-alone automated segmentation application called *Fragfinder* [30] was developed using MATLAB® (MathWorks Inc.) and the algorithms from its Image Processing Toolbox. The *Fragfinder* interface (Figure 6) consists of four auxiliary sections: image data, test conditions, processing, and info.

TABLE II. SIEMENS CT SCANNER AS+ SPECIFICATIONS AND OPTIMAL VALUES.

Parameters	Range of values	Optimal values
X-ray source voltage	70kV, 80kV, 100kV, 120kV, 140kV	140kV
X-ray source amperage	Single source 20 - 1300 mAs	330mAs
Field of view	5 – 70cm (extended field of view)	2x 45cm
Pitch	0.095 – 1.5	0.5
Detector collimation	16x0.6mm to 128x0.6mm	128 x 0.6mm
Reconstruction matrix size	Fixed at 512x512	512x512
Reconstruction increment width	0.1 – 20mm	0.6mm
Minimum voxel size	100x100x400µm	-
Maximum temporal resolution	150ms	-
Contrast resolution	1HU = 0.001g/cm^3	-

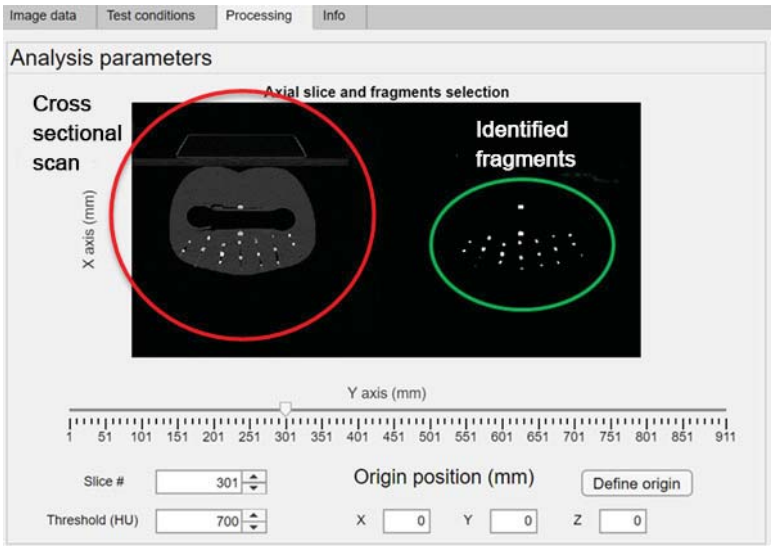

Figure 6. *Fragfinder* interface for automatic CT-scan analysis.

Currently, *Fragfinder* utilizes a global threshold based segmentation technique [31] for partitioning every pixel of the digital images into identifiable objects where the user specifies the single HU threshold value and can then visually see the effect on the number of identified fragments.

Once the segmentation process is completed, the identified objects can then be counted, and the following properties computed: 3D location, principal dimensions, volume (*Vol*), external surface area (*Es*), DoP (normal and line of sight, Figure 1), flatness, elongation, and sphericity. The dimensionless shape factor (*Sf*) [32] is calculated using equation 1 where the mean presented area (*Ap*) is equal to one quarter of *Es* using Cauchy formula for randomly oriented convex solids (unstable/tumbling fragment).

$$Sf = \frac{Ap}{Vo^{2/3}} = \frac{\frac{Es}{4}}{Vo^{2/3}} \qquad (1)$$

Wound cavity volume is calculated as the product of DoP and *Ap*. The average HU value of each fragment is used for attributing the likely material composition based on the closest known HU value for the materials specified. Fragment mass is then calculated using the corresponding material density and fragment volume. *Fragfinder* also computes the trajectory of each fragment from the specified explosion origin (Figure 7 left) and the related line of sight DoP (L-DoP, Figure 1) using the target spatial orientation. Impact velocity is computed using the user provided DoP calibration equation and L-DoP. Ballistic dose is then derived from the estimated fragment mass and velocity. Subzones (Figure 7 right) within a target can also be defined allowing for a refined analysis of PPE with non-uniform protection. The number, mass, cavity volume, and ballistic dose for each fragment are then cumulated as global injury metrics. Total cavity volume can be shown to be a good proxy of the transmitted ejecta impulse when using a velocity- normalized DoP linear fit (Figure 2 left) and a sphere of same volume for each fragment. The Kokinakis equations [20] developed for steel fragments are used to compute individual *Pi* values from the ballistic dose along with a binomial product to obtain the total *Pi* for all embedded fragments, i.e. no synergistic effects being considered. For addressing non-steel

fragments, a correction is applied by calculating the reduced velocity of an equivalent spherical steel (7.8g/cm^3 density) fragment of same mass and DoP but of smaller diameter. The analysis is completed in a few minutes.

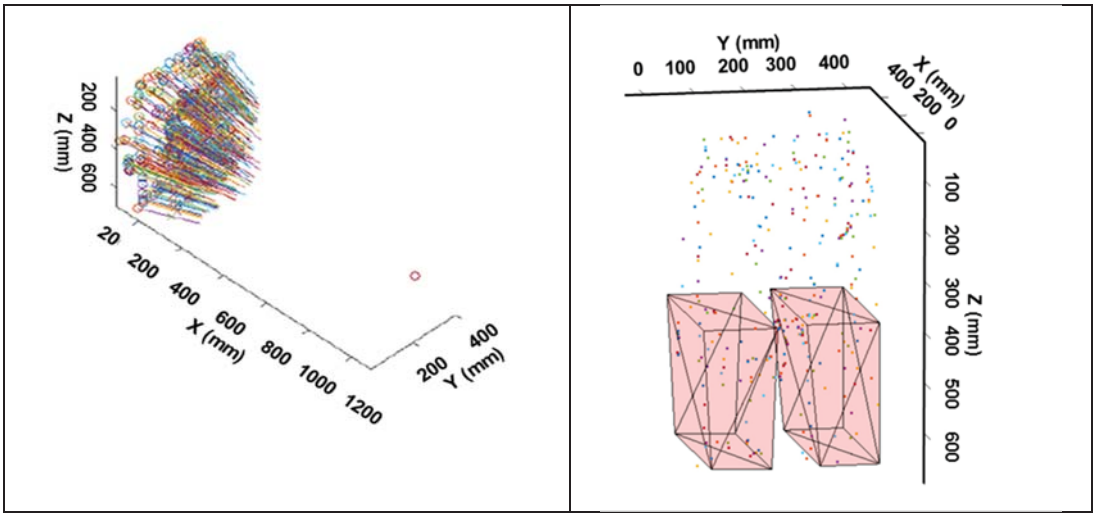

Figure 7. Fragfinder gel torso target analysis: fragment origin/trajectory (left), leg zone (right).

EXPERIMENTAL RESULTS

For the foam and gel calibration targets, *FragFinder* was able to detect all of the 320 and 159 embedded fragments, respectively. For the fragment center of gravity (CG) location, the mean resolution obtained for the 20 different shapes in each layer was less than 2 mm for the foam target. For the volume, the relative error was based on the absolute value of the difference between the estimated and the measured volume. The largest relative errors were observed for the smallest cylinder (15.7 %) with a volume of 16 mm^3 and the smallest sphere (25.5 %) with volume of 9 mm^3 (TABLE IIII, Figure 9). The average relative error for all 20 object shapes was 5.9 %.

The largest absolute error was observed for the large rectangular prism (31.3 mm^3, data not shown). From our observations, the mean absolute positive error for all shapes was strongly correlated to the fragment mean presented area (*Ap*). The ratio of the mean absolute positive error (mm^3) divided by *Ap* (mm^2) was always in the range of 0.1 to 0.4 mm (TABLE IIII).

This quantifies one of the limiting parameter of the method and can be interpreted as the "thickness of incertitude" related to the discrimination process along the object external skin during segmentation.

TABLE III. RELATIVE AND ABSOLUTE NORMALISED VOLUME ERROR.

Size:	Small		Intermediate		Large	
Shape	Err-Vol (%)	Err-Ap (mm)	Err-Vol (%)	Err-Ap (mm)	Err-Vol (%)	Err-Ap (mm)
Cylinder small	15.7	0.2	11.7	0.2	9.8	0.2
Cylinder large	7.6	0.2	6.7	0.2	4.3	0.2
Cube	6.5	0.2	2.8	0.1	4.5	0.2
Hex. prism	6.5	0.2	6.4	0.2	5.1	0.2
Rect. prism	7.9	0.2	12.6	0.4	-	-
Sphere	25.5	0.3	11.5	0.2	9.7	0.3

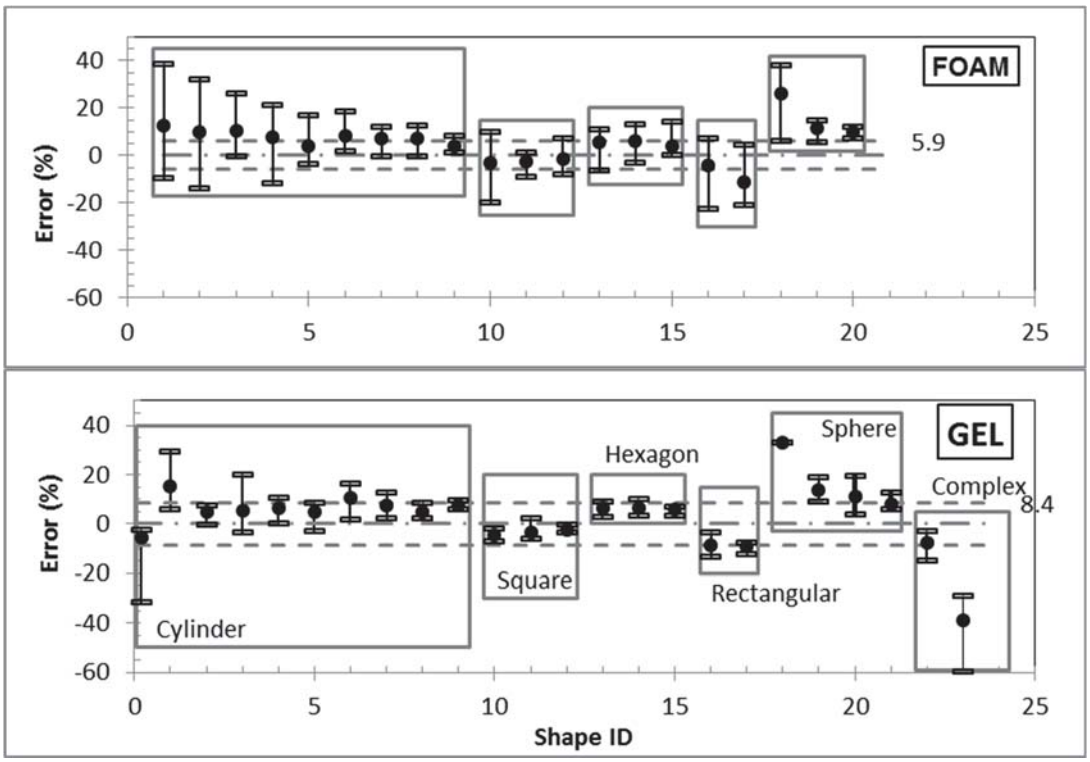

Figure 8. Volume relative errors for foam (top) and gel targets (bottom), overall average: dash lines.

A portion of the error on the estimated volume can be attributed to the voxel size and shape used in the analysis (0.6 mm cube), as illustrated in Figure 9 for the smallest sphere and the large rectangular prism. For the sphere and cylinder shapes, the relative error is larger for smaller objects since the resolution is independent of the object size.

The precision on the estimated shape factor is shown in Figure 10. In all cases the shape factor is overestimated due to the digitation pattern producing jagged contours, which artificially increases the surface areas.

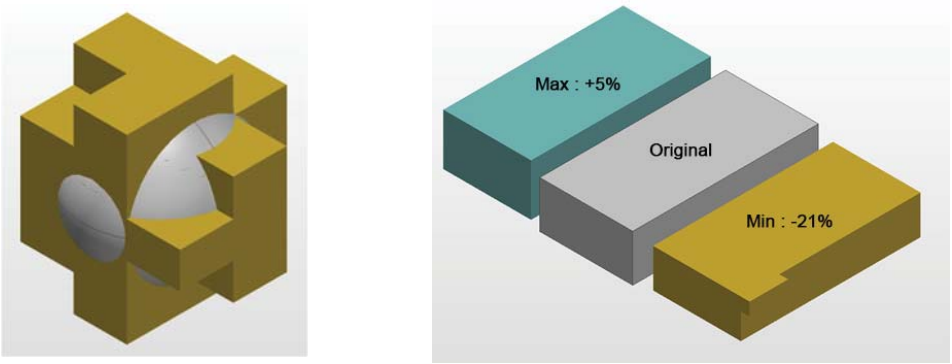

Figure 9. Voxel digitalization vs true shape of a 2.5mm-glass sphere (left) and a rectangular prism (right).

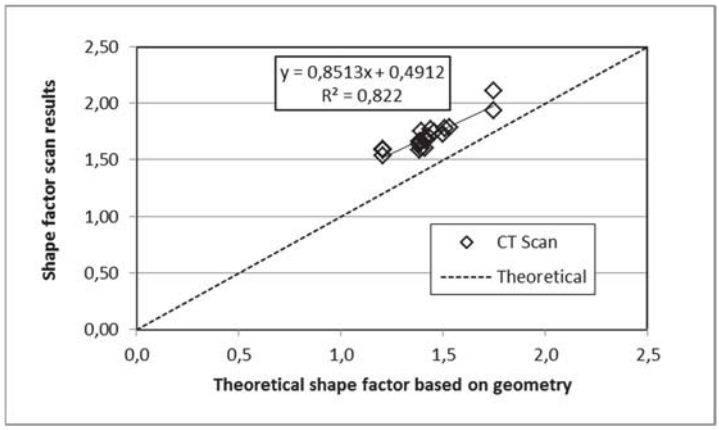

Figure 10. Comparison of shape factors based on geometry versus digitized ones.

For the torso gel target, a similar trend was observed (overall average of 8.4%) for the various shapes (lower part of Figure 8). The largest mean error (-40%) was observed for the complex shape (shape ID 23) and is due to the cavity at the rear part of the bookbinding screw post, where the wall thickness is close to the voxel size.

For the plywood calibration target with low and high density fragments in the mixed material section, the volume analysis with *Fragfinder* was more arduous due to the presence of bright star-shape streaks (glare effects in Figure 11). These artifacts are caused by the greater attenuation of high density metallic objects, leading to beam hardening of the polychromatic X-ray source and scattering along the object edges. Their presence makes image pixel classification and discrimination more difficult. Although many techniques [33] have been proposed for artifact reduction, it still remains a challenging problem. The correlation between the measured and the real object volume is shown in Figure 12. It can be seen that some of the objects contained in this target had a much larger volume than in the two previous calibration targets. For low density materials and larger object sizes, the correlation is adequate. The largest errors illustrated by the grey dashed lines are observed for the tungsten objects. The shape resolution is illustrated in Figure 13 for 7.62mm FSP, a wing nut.

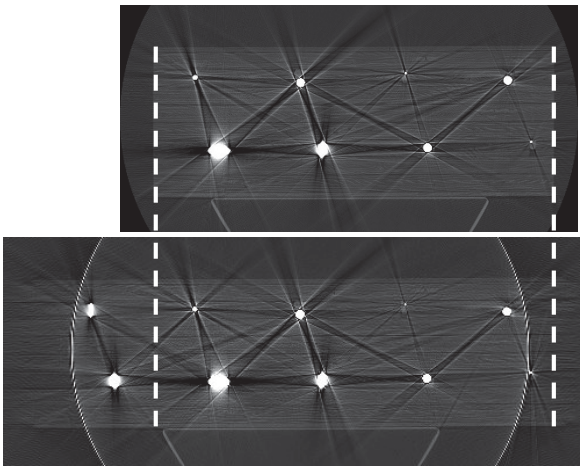

Figure 11. Reconstructed images of plywood calibration target (full width: bottom; reduced width: top).

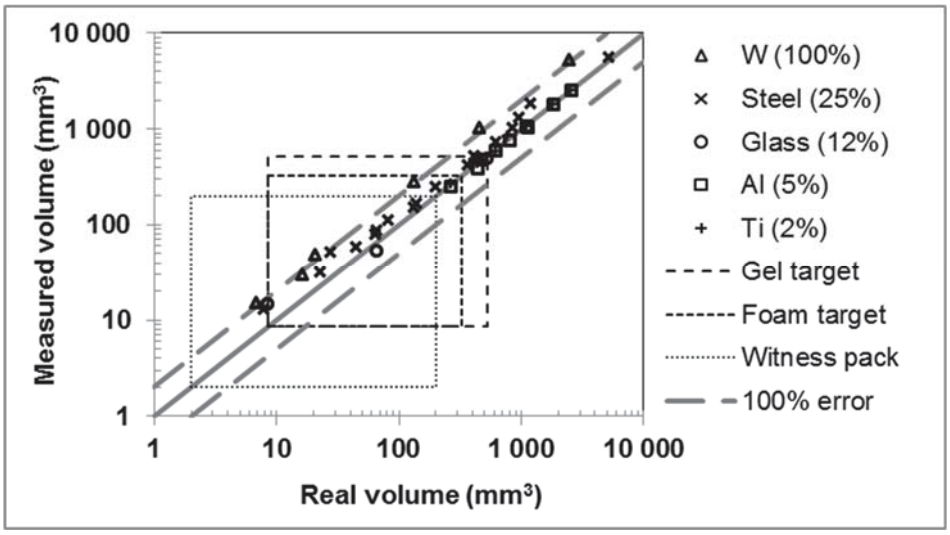

Figure 12. Real and measured volume of objects in plywood calibration target.

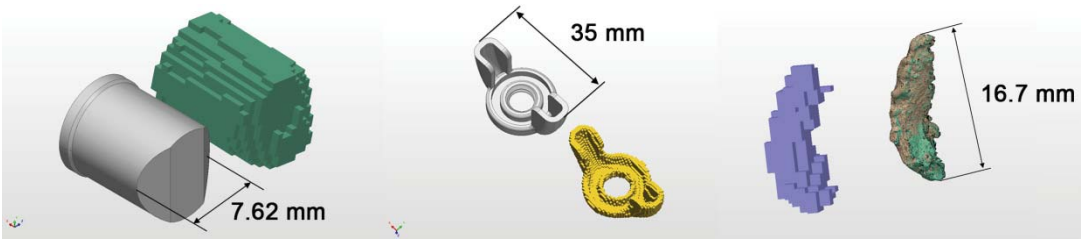

Figure 13. Real shapes and voxel meshes: FSP (left), wing nut (center) and munition fragment (right).

For the plywood witness pack, the analysis is still on-going. Only three real fragments were found at the upper end of the volume range indicated by the dotted frame in Figure 12. Although most of the fragments were of small size, their shape was still relatively well captured (right part of Figure 13).

CONCLUSIONS

The results obtained with the foam and gel anthropomorphic calibration targets demonstrated that XCT allows for the rapid non-invasive detection and in-situ characterization of embedded fragments. Volumetric measurements were within 8% of the true values and 3D location was measured with a resolution of 2 mm, i.e. close to the voxel size used. The ability to rapidly conduct the analysis on 3D complex shapes is a key advantage of the XCT technique over the manual recovery of fragments, which is limited to simpler/layered geometry witness/surrogate systems. For the plywood targets, good correlation was obtained for the lower density fragments (glass and aluminum). For the CT-scanner used herein, the maximum width of the witness pack need to be less than 440 mm since lower resolution is obtained when using the extended field of view. The metal artifacts encountered with the steel and tungsten fragments prevented precise measurement of fragment volumes using the current algorithm within *Fragfinder*. Future efforts will explore optimizing the image

segmentation process using both local and hybrid thresholds (hybrid method) to deal with metal artifacts. For smaller fragments, better spatial resolution would be achievable by performing the reconstruction process on a number of smaller size contiguous sample zones. The reduced display field of views for each zone would lead to smaller pixel sizes. The reconstruction data for each zone would then need to be recombined into a single 3D matrix with an increased pixel density for subsequent segmentation processing. For obtaining higher precision, the use of micro/nano CT scanners with resolution of 0.5 μm or less would also be an option to consider.

ACKNOWLEDGEMENT

The authors would like to acknowledge the support of the Land Engineering Support Centre (LESC) for this study performed under DRDC's Soldier System Effectiveness (SoSE) and Land Operational Vehicle (LOV) projects. The authors also thank Louis-Frédéric Daigle (INRS) for CT-Scans acquisitions, Philippe Lettelier (INRS) for helping with the *Fragfinder* development, Ed Fournier and Stephane Magnan from Biokinetics for their contribution on the injury analysis and Guillaume Roy and Bernard Paquette from DRDC the preparation and analysis of the calibration targets.

REFERENCES

1. US Army. 1993. "ITOP-4.2.813 - Static Testing of High Explosive Munitions for Obtaining Fragment Spatial Distribution", Test and Evaluation Command, AD-A262 272.
2. Kulaga, A, Myers,T. and G. Patrick. 2014. "Design Upgrade of the Plywood-Penetration Mannequin", Proceedings 28th International Symposium on Ballistics, Atlanta, GA, USA.
3. Kaufman M. and L. Moss. 2015. "Reassessing the Representative Heuristic of the Plywood Ballistic Mannequin Used in Live-Fire Testing", US Army Res. Lab., MD, USA, Report TR-7274.
4. Jordan, B., and C. Naito. 2010. "Calculating fragment impact velocity from penetration data", in *Int. J. of Impact Eng.*, vol. 37(5), pp. 530-536.
5. Eberius, N., and P. Gillich. 2010. "Survivability Analysis for the Evaluation of Personnel in Body Armor", Proceedings PASS 2010, Quebec City, QC, CA.
6. Saunders, C., and D. Carr. 2018. "Towards developing a test method for military pelvic protection", in *The Journal of the Textile Institute*, vol. 109(10), pp. 1374-1380.
7. Bagchi, A., et al. 2014, "Novel Methodology to Quantify Performance of Protective Undergarments, Overgarments and Outergarments in Blast Tests", PASS 2014, Cambridge, UK.
8. Freitas, C.J., et al. 2014. "Threat Characterization Methodology for IED Post-Detonation Environments to Dismounted Warfighters", Proceedings PASS 2014, Cambridge, UK.
9. van der Jagt-Deutekom, M.J., and T. Westerhof. 2018. "Assessment of the secondary fragments from buried explosives", Proceedings PASS 2018, Washington D.C, USA.
10. Mah, J., et al. 2006. "Damage caused by soil debris ejecta from buried IED anti-personnel mines, Proceedings PASS 2006, Leeds, UK.
11. Moholkar. N. 2018. "Characterizing the Ballistic Performance of Polystyrene Foam for the Development of Body Armor Mannequin", US Army Res. Lab., report ARL-CR-0835, MD, USA.
12. Sanborna, K., et al. 2019. "Ballistic performance of Cross-laminated Timber (CLT)", in *Int. J. of Impact Eng*., vol.128, pp 11–23.
13. Bosik, A., et al. 2002. "Initial Findings on the development of test procedures for multi-hit testing of body armour", Proceedings PASS 2002, The Hague, the Netherlands.
14. Zhang, G.M., et al. 2008. "Effect of frame size, frame type, and clamping pressure on the ballistic performance of soft body armor", in *Compos. Part B Eng*., vol. 39, no. 3, pp. 476–489.

15. Ouellet, S. and G. Pageau. 2018. “Development of a Simplified Torso Surrogate based on selected Biofidelity Corridors for the Assessment of the Ballistic Performance of Soft Body Armor”, Proceedings IRCOBI-2018 Conference, Athens, Greece.
16. Wijk, G. 2001. “Sphere penetration into gelatin and board”, Proceedings 19th International Symposium of Ballistics, Interlaken, Switzerland.
17. Heine, A., and M. Wickert. 2015. “Scale-independent description of the rigid-body penetration of spherical projectiles into semi-infinite adobe targets”, Int. J. of Impact Eng., vol. 75, pp. 27-29
18. Cunniff, P.M. 2014. “A Method to Describe the Statistical Aspects of Armor Penetration, Human Vulnerability and Lethality due to Fragmenting Munitions”, Proceedings 28th International Symposium on Ballistics, Atlanta, GA, USA.
19. Sperrazza, J., and W. Kokinakis. 1968. “Ballistic limits of tissue and clothing”, New York Academy of Sciences, vol. 152(1), pp.163–167.
20. Eisler, R., et al. 2001. “Casualty Assessments of Penetrating Wounds from Ballistic Trauma”, NATICK Soldier Center Report TR-01/011.
21. Kokinakis, W. and J. Sperrazza. 1965. “Criteria for Incapacitating Soldiers with Fragments and Flechettes”. BRL Report 1269. Ballistic Research Laboratory, USA.
22. Schmitt, R., and C. Niggemann. 2010. “Uncertainty in measurement for x-ray-computed tomography using calibrated work pieces” in *Meas. Sci. and Tech.*, vol. 21 (5), pp.4008-17.
23. Sun, W., S.B. Brown, and R.K. Leach. 2012. “An overview of industrial X-ray computed tomography”, National Physical Laboratory NPL Report ENG 32.
24. Rutty, G.N., et al. 2008. “The role of computed tomography in terminal ballistic analysis”. In *Int. J. Legal Med*., vol. 122(1), pp. 1-5.
25. Breeze, J., et al. 2016. “Determining the dimensions of essential medical coverage required by military body armour plates utilizing Computed Tomography”, *Injury,* vol. 47(9), pp. 1932-1938.
26. Tsiatis, N. et al. 2015. “The application of computed tomography in wound ballistics research”, in *J. Phys.: Conf. Ser*. vol. 637, conf. 1 (637 012029).
27. Wells, J. 2009. “In-Situ Fragment Analysis with X-Ray Computed Tomography (XCT)”, Proceedings Advances in Ceramic Armor III conference, Vol. 8(5), pp. 181-192.
28. Zellnera, M.B., and K. Champley. 2019. “Development of a computed tomography system capable of tracking high velocity unbounded material through a reconstruction volume”, in *Int. J. of Impact Eng*. vol. 129 pp. 26–35.
29. Boas, F.E., and D. Fleischmann. 2012. “CT artifacts: Causes and reduction techniques”, in *Imaging in Medicine*, vol. 4(2), pp. 229-240.
30. DesRoches, et al. 2019. “FragFinder – User manual (Version 1.7)”, INRS CT Scan lab, June 2019
31. Zaitouna, N.M., and M.J. Aqelb. 2015. “Survey on Image Segmentation Techniques”, in *Procedia Computer Science*, vol. 65, pp. 797-806.
32. Saucier R. 2016. “Shape Factor Modeling and Simulation”, US Army Res. Lab., Report TR-7707.
33. Chen, M., and X. Dimeng. 2019. “An Analytical Method for Reducing Metal Artifacts in X-Ray CT Images”, in *Mathematical Problems in Engineering*, HindawiArticle ID 2351878.